Direct imaging of traveling Lamb waves in plates using photorefractive dynamic holography

K. L. Telschow, V. A. Deason, R. S. Schley and S. M. Watson

Idaho National Engineering and Environmental Laboratory

Lockheed Martin Idaho Technologies Co.

P.O. Box 1625

Idaho Falls, ID 83415-2209

ABSTRACT

Anisotropic stiffness properties of sheet materials can be determined by measuring the propagation of Lamb waves in different directions, but this typically requires multiple positioning of a suitable transducer at several points or scanning over the area of the sample plate. A laser imaging approach is presented that utilizes the adaptive property of photorefractive materials to produce a real-time measurement of the antisymmetric Lamb traveling wave displacement and phase in all planar directions simultaneously without scanning. Continuous excitation and lock-in methodology is employed enabling the data to be recorded and displayed by a video camera. Analysis of the image produces a direct quantitative determination of the phase velocity in all directions showing plate stiffness anisotropy in the plane. The method is applicable to materials that scatter light diffusely and provides quantitative imaging of the dynamic surface motion exhibited by traveling elastic waves. A description is given of this imaging process and, for the first time, its ability to perform lock-in measurement of elastic wave displacement amplitude and phase.

INTRODUCTION

    Many optical techniques for measuring ultrasonic motion at surfaces have been developed for use

in applications such as vibration measurement and laser ultrasonics. Most of these methods have

similar sensitivities and are based on time domain processing using homodyne, heterodyne, Fabry-

Perot[1], and, more recently, photorefractive interferometry[2]. Generally, the methods described above

do not allow measurement at more than one surface point simultaneously, requiring multiple beam

movements or scanning in order to produce images of ultrasonic motion over an extended area.

Electronic speckle interferometry and shearography do provide images of vibrational motion over

large surface areas. This method has proven very durable in the field for large displacement

amplitudes and a sensitivity of 1/3000 of the optical wavelength has been demonstrated under

laboratory conditions.[3] Full-field imaging of traveling ultrasonic waves using digital shearography

has been recently reported with sensitivity in the nanometer range.[4] With this method, optical

interference occurs at the photodetector surface of the camera that records the speckle image from

the sample surface.   Multiple image frames are typically recorded and processed in a computer to

produce an output proportional to sample surface displacement. This paper discusses a powerful

alternative method that utilizes the photorefractive effect in optically nonlinear materials to perform

adaptive optical interferometry in an imaging mode.[5,6] Optical interference occurs within the

photorefractive material with this technique and the output is an optical image whose intensity

distribution is directly proportional to the sample surface vibration amplitude for small ultrasonic

displacements. Utilizing this approach, no post-processing of the data recorded by a video camera is

required to produce images of the surface vibration amplitude over large areas. The application of

this approach to imaging of standing wave resonant motion in plates has been previously

described.[7,8,9] This paper describes results of an investigation into the fundamental operation and

application of this technique to nonstationary waveforms through imaging of traveling Lamb waves

in plates.[10] The ability to measure nonstationary waveforms not only at single points but also as an image over a surface comes from the inherent lock-in measurement process occurring. This recording mechanism is developed theoretically as well as experimentally here, for the first time, for imaging of flexural wave propagation in isotropic plates. Application to imaging flexural wave propagation in anisotropic plates is also presented. A benefit of the imaging approach is developed from the Fourier transform of the recorded wavefront that produces a mapping of the propagation wavevector in all planar directions as a single image. This mapping yields information about the elastic symmetry of the wave propagation and, therefore, the material microstructure directly.

BACKGROUND

   Photorefractivity[5]refers to that process where optical excitation and transport of electrically charged carriers within select nonlinear optical materials produces an optical diffraction grating from the interference pattern developed inside the material.   A spatial and temporal charge distribution results in the photorefractive material that reflects the optical phase information impressed onto the optical signal beam by the vibrating sample surface. Several optical frequency domain measurement methods of vibration have been proposed using photorefractive two and four-wave mixing in select materials.[11,12] These provide a time averaged response that is a nonlinear function of the specimen vibration displacement amplitude. A method using an unconventional photorefractive process has been reported that provides output linear with the vibration displacement amplitude, but it is limited to a select group of materials.[13] The method reported here utilizes the normal photorefractive effect to produce an optical grating at a fixed beat frequency between the phase modulated signal and reference beams. It can be used in a manner that directly measures vibration amplitude and phase with a response proportional to the Bessel function of order one, providing a linear output for small amplitudes. The method accommodates rough surfaces, exhibits a flat frequency response above the

photorefractive cutoff frequency and can be used for detecting both standing and traveling waves. In this paper, the underlying physics of the optical detection process is developed and application of the method to full-field imaging of traveling Lamb waves in plates with isotropic and anisotropic stiffness properties is presented.

EXPERIMENTAL METHOD

The experimental setup for vibration detection is shown in figure 1. A solid state laser source at 532 nm was split into two legs forming the signal and reference beams. The signal beam was reflected off traveling waves produced at the surface of a nickel plate driven at its center by a continuously excited piezoelectric transducer. The excited traveling waves occurring on the plate surface produced a phase modulation δ_{sig} of the signal beam. The reference beam was phase modulated by an electro-optic modulator at a fixed modulation depth δ_{ref} . The photorefractive material was from single crystal Bismuth Silicon Oxide (BSO) of size 10 mm by 10 mm by 2.25 mm and cut along the <001> and <011> directions. The measured time constant was 0.01 ms. The modulated beams were combined and interfered inside the BSO photorefractive crystal utilizing an external angle $2\theta = 55$ degrees between the beams in order to produce a large response for operation in the diffusive charge transport regime. The refractive index grating produced within the photorefractive material can be readout by four-wave or two-wave mixing techniques.

In the four-wave mixing configuration, the reference beam was reflected back into the crystal along a counter-propagating path that matched the Bragg angle of the photorefractive grating in the medium. The vibration induced optical phase grating was read out by the resulting diffracted reference beam, or conjugate signal beam, that propagated backward along the signal beam leg and was detected by deflecting it with a beamsplitter (not shown) toward a photodetector. Subsequently,

when only one detection point was being interrogated, the photodetector signal was processed with conventional electrical lock-in methods to increase the measurement signal to noise ratio through utilizing a small detection bandwidth. A video charge-coupled device (CCD) camera was employed to record the demodulated optical phase grating and produce images of the elastic displacement wavefront over the surface of the plate. Four-wave mixing isolated the signal beam phase information very effectively from the transmitted signal beam.

A significant drawback of the four-wave mixing approach is the low output intensity of the readout process. This was improved by employing a two-wave approach that recorded the forward diffracted beam enhanced by the gain of the two-wave mixing process. However, there was also a significant component of the directly transmitted signal beam that had to be discriminated against in order to achieve maximum sensitivity. Optically active photorefractive materials, in this case BSO, offer a means for providing the needed discrimination through optical activity and anisotropic self-diffraction, which produce a rotation in the linear polarization of the diffracted reference beam with respect to that of the transmitted signal beam. By using an appropriate thickness of the photorefractive crystal, it was possible to achieve a nearly 90° polarization shift between the two beams.[14] This allowed reduction of the directly transmitted signal beam through the use of high extinction ratio polarizers. The resulting intensity of the diffracted reference beam was dependent on the vibration displacement and temporally modulated at the frequency difference between the mixing waves in a manner analogous to the four-wave mixing case. As before, only the output intensity need be measured to obtain both the vibration amplitude and phase, thereby allowing direct imaging and ease of interpretation.

FLEXURAL WAVE DISPLACEMENT DISTRIBUTION

The mechanism that allows recording of traveling wave displacements can be illustrated by considering a traveling flexural wave in a plate. The classical differential equation of motion for the out-of-plane displacement of an isotropic homogeneous plate driven by a force per unit area of $f_p(\rho,t)$ is given by[15]

$$D\nabla^4\xi + \sigma\frac{\partial^2\xi}{\partial t^2} = f_p(\rho,t) \tag{1}$$

where $D \equiv \dfrac{Eh^3}{12(1-s^2)}$ is the bending stiffness of the plate, $\sigma \equiv \rho_m h$ the mass density per unit area, ρ_m = the mass density of the material, s = Poisson's ratio, E = Young's modulus, h = the plate thickness, ξ is the displacement normal to the plate surface and ρ is the radial spatial coordinate. Eqn. 1 is valid at low frequencies where the elastic wavelength (λ_a) is much larger than the plate thickness, i.e. $k_a = \dfrac{2\pi}{\lambda_a}$, for $k_a h \ll 1 \Rightarrow h \ll \dfrac{\lambda_a}{2\pi}$ and approximates the lowest antisymmetric Lamb or flexural wave mode. Consider a traveling flexural wave excited at a single point on the plate by a piezoelectric transducer undergoing continuous oscillation with frequency $\dfrac{\omega_s}{2\pi}$ and phase φ_s producing a point force per unit area on the plate of $f_p(\rho,t) = \mathrm{Re}\left[F_0\dfrac{\delta(\rho)}{2\pi\rho}e^{-i(\omega_s t + \varphi_s)}\right]$, where the amplitude of the total force applied to the plate is F_0 and $\delta(x)$ is the Dirac delta function.

Eqn. 1 can be rewritten utilizing $\xi(\rho,t) = \xi_\rho(\rho)e^{-i(\omega_s t + \varphi_s)}$, where $\xi_\rho(\rho)$ is the complex displacement amplitude, as follows

$$(\nabla^2 - k_a^2)(\nabla^2 + k_a^2)\xi_\rho(\rho) = \frac{F_0}{2\pi D}\frac{\delta(\rho)}{\rho} \tag{2}$$

where $k_a^4 \equiv \dfrac{\sigma\omega^2}{D}$. Since Eqn. 2 is a fourth order differential equation, in addition to the two

propagating wave modes, two non-propagating heavily damped modes must also be included in order

to form a complete solution satisfying the boundary conditions. The solution can be found by

adopting the time dependence of the forcing function along with applying the 2-dimensional spatial

Fourier transform, which, for a circularly symmetric function, can be expressed in terms of the

Hankel transform of order zero as[16]

$$\tilde{g}(k) = 2\pi\int_0^\infty g(\rho)J_0(k\rho)\rho d\rho \qquad \Leftrightarrow \qquad g(\rho) = \frac{1}{2\pi}\int_0^\infty \tilde{g}(k)J_0(k\rho)kdk \tag{3}$$

with $\dfrac{\delta(\rho - \rho')}{\rho} = \displaystyle\int_0^\infty J_0(k\rho')J_0(k\rho)kdk$, and $\dfrac{\delta(k - k')}{k} = \displaystyle\int_0^\infty J_0(k'\rho)J_0(k\rho)\rho d\rho$. Applying the

transform to Eqn. 2 and using the orthogonality of the Bessel functions yields the radial solution in

the Fourier domain as

$$\tilde{\xi}_\rho(k) = \frac{F_0}{D}\left[\frac{1}{(k^2 - k_a^2)(k^2 + k_a^2)}\right]. \tag{4}$$

The resultant waveform traveling outward from the excitation point in the spatial domain is obtained by the inverse transform according to

$$\xi_\rho(\rho) = \frac{F_0}{2\pi D} \int_0^\infty \left[\frac{J_0(k\rho)}{(k^2 - k_a^2)(k^2 + k_a^2)} \right] k\,dk \tag{5}$$

which can be integrated using the relation $\int_0^\infty \frac{J_0(x\rho)x\,dx}{(x^2 + k^2)} = K_0(k\rho)$,[17] where $K_0(x)$ is a Modified Bessel function of the second kind. The resultant traveling wave solution is given by[18]

$$\xi(\rho,t) = \mathrm{Re}\left\{ i\xi_0 \, [H_0^1(k_a\rho) - H_0^1(ik_a\rho)] e^{-i(\omega_s t + \varphi_s)} \right\} \tag{6}$$

where $\xi_0 \equiv \dfrac{F_0}{8\omega\sqrt{D\sigma}}$, $k_a = \dfrac{2\pi}{\lambda_a}$, $\lambda_a = \dfrac{c_a}{\omega_s}$ is the antisymmetric traveling mode wavelength with phase velocity c_a and $H_0^1(x) = J_0(x) + iN_0(x)$ is the Hankel function of order zero representing a wave traveling outward from the origin. A central conclusion of this research is that the optical imaging approach described measures both the elastic wave amplitude and phase over the plate surface simultaneously in a manner similar to electrical signal lock-in detection. The explicit separation of the flexural wave displacement into terms depicting the elastic wave amplitude and phase is not readily apparent from Eqn. 6. However, this separation can be achieved near the origin and far away by expanding the Hankel functions. Near the origin, the Bessel functions can be

expanded as $J_0(x) \underset{x\to 0}{\to} 1 - \dfrac{x^2}{4}$, $N_0(x) \underset{x\to 0}{\to} \dfrac{2}{\pi}[\ln(\dfrac{x}{2}) + \gamma]$, $\gamma = 0.5772...$ to show that

$\lim_{x \to 0} [H_0^1(x) - H_0^1(ix)] = 1$, designating ξ_0 as the displacement amplitude at the source point.

Another way of writing the solution, using the relation $K_0(x) = \dfrac{\pi i}{2} H_0^1(ix)$, is

$$\xi(\rho,t) = \xi_0 \left[J_0(k_a \rho) \sin(\omega_s t + \varphi_s) - \left[N_0(k_a \rho) + \frac{2}{\pi} K_0(k_a \rho) \right] \cos(\omega_s t + \varphi_s) \right]. \quad (7)$$

which explicitly shows the traveling wave near and far field behavior as

$$\xi(\rho,t) \xrightarrow[k_a \rho \to 0]{} \xi_0 \sin(\omega_s t + \varphi_s), \qquad \xi(\rho,t) \xrightarrow[k_a \rho \to \infty]{} \xi_0 \sqrt{\frac{2}{\pi k_a \rho}} \sin(\omega_s t + \varphi_s - k_a \rho + \frac{\pi}{4}).$$

These expressions show that the displacement at the origin is ξ_0 and that as the elastic wave travels

away from the origin, its phase increases linearly with radial distance. The normal lock-in method

allows one to detemine the flexural wave amplitude and phase separately and then reconstruct the

displacement completely at any point. The next section shows this procedure explicitly for the

photorefractive detection methodology.

PHOTOREFRACTIVE TRAVELING WAVE DETECTION

The method by which the photorefractive process demodulates the optical phase information can

be illustrated by considering an approximation to the two-wave & four-wave mixing processes. The

integral form of the Hankel function,[19]

$$H_0^1(x) = \sqrt{\frac{2}{\pi x}} e^{i(x - \frac{\pi}{4})} \int_0^\infty \frac{e^{-u}}{\sqrt{\pi u}} (1 + \frac{iu}{2x})^{-\frac{1}{2}} du = h_0(x) e^{i(x - \frac{\pi}{4})}, \text{ can be used to write Eqn. 6 for the}$$

traveling wave displacement as

$$\xi(\rho,t) = \text{Re}\left[i\xi_0 |h(k_a\rho)| e^{i\Phi_a} e^{i(k_a\rho - \frac{\pi}{4} - \omega_s t - \varphi_s)} \right] \qquad (8)$$

where $|h(k_a\rho)| e^{i\Phi_a} \equiv h_0(k_a\rho) - h_0(ik_a\rho)e^{-k_a\rho(1+i)}$. The optical phase shift of the signal

beam, referring to Figure 1 and assuming normal incidence, $\zeta = 0$, produced by the traveling wave

can be described using Eqn. 8, with $\chi(\rho) = (k_a\rho - \frac{\pi}{4} + \Phi_a)$, as

$$\delta_{sig}(\rho,t) = \frac{4\pi\xi(\rho,\omega_s t + \varphi_s - \chi(\rho))}{\lambda} = \frac{4\pi\xi_0}{\lambda}|h(k_a\rho)|\sin(\omega_s t + \varphi_s - \chi(\rho)). \qquad (9)$$

Using the relation $e^{ix\sin(\theta)} = \sum\limits_{n=-\infty}^{n=\infty} J_n(x)e^{in\theta}$, the electric field amplitude of the optical signal

beam can be represented, referring to figure 1, as

$$\begin{aligned} A_s(r,t) &= \sqrt{I_s}\, e^{i(\vec{k}_s \cdot \vec{R}_s - 2\pi vt + \delta_{sig}(\rho,t))} \\ &= \sqrt{I_s}\, e^{i(\vec{k}_s \cdot \vec{R}_s - 2\pi vt)} e^{i\delta_{sig0}\sin(\omega_s t + \varphi_s - \chi(\rho))} \\ &= \sqrt{I_s}\, e^{i(\vec{k}_s \cdot \vec{R}_s - 2\pi vt)} \sum\limits_{n=-\infty}^{n=\infty} J_n(\delta_{sig0})e^{in(\omega_s t + \varphi_s - \chi(\rho))} \end{aligned} \qquad (10)$$

where $\delta_{sig0} = \frac{4\pi\xi_0}{\lambda}|h(k_a\rho)|$, $\vec{R}_s = \vec{r} + \vec{r}_s$, I_s the optical signal beam intensity, k_s is the optical

signal beam wavevector and v is the laser optical frequency. The reference beam is phase modulated

with magnitude δ_{ref0}, at the frequency $\dfrac{\omega_r}{2\pi}$ and phase φ_r by an electro-optic modulator (EOM)

according to $\delta_{ref} = \delta_{ref0}\sin(\omega_r t + \varphi_r)$, which produces a reference beam amplitude

$$
\begin{aligned}
A_r(r,t) &= \sqrt{I_r}\, e^{i(\vec{k}_r \cdot \vec{R}_r - 2\pi vt + \delta_{ref})} \\
&= \sqrt{I_r}\, e^{i(\vec{k}_r \cdot \vec{R}_r - 2\pi vt)} \sum_{m=-\infty}^{\infty} J_m(\delta_{ref0}) e^{im(\omega_r t + \varphi_r)}
\end{aligned}
\tag{11}
$$

where $\vec{R}_r = \vec{r} + \vec{r}_r$, I_r the optical reference beam intensity, k_r is the optical reference beam

wavevector .

Interference inside the crystal produces a spatially and temporally modulated intensity pattern, assuming the polarizations of the signal and reference beams are the same, as

$$
I = I_0\left[1 + M\cos(\vec{K}\cdot\vec{r} + \Sigma + \delta_{sig} - \delta_{ref})\right], \quad I_0 = I_s + I_r, \quad M = \frac{2\sqrt{I_s I_r}}{I_0}, \tag{12}
$$

where $\vec{K} = \vec{k}_s - \vec{k}_r$ is the grating wavevector and $\Sigma = \vec{k}_s \cdot \vec{r}_s - \vec{k}_r \cdot \vec{r}_r$ accounts for path length

differences between the two beams. The interference intensity distribution within the crystal generates

a corresponding space charge electric field distribution. The dynamic behavior of this field is

controlled by the charge carrier mobility and trapping that produces, in the diffusive operation

regime, a single relaxation time response given by[20]

$$
\frac{\partial E_{sc}}{\partial t} + \frac{E_{sc}}{\tau} = \frac{iE_q}{\tau}\frac{2A_s \cdot A_r^*}{I_0} \tag{13}
$$

where τ is the material response time. The maximum achievable space-charge field, $E_q = \dfrac{qN_A\Lambda}{2\pi\varepsilon}$, is controlled by the concentration of available charge trapping sites N_A, the fringe spacing $\Lambda = \dfrac{2\pi}{K}$, the carrier charge q and the permittivity of the medium ε. Using Eqn.s 10 through 12, the interference term in Eqn. 13 becomes

$$\frac{2A_s \cdot A_r^*}{I_0} = M \sum_{n,m=-\infty}^{n,m=\infty} J_n(\delta_{sig0}) J_m(\delta_{ref0}) e^{i[\vec{K}\cdot\vec{r}+\Sigma+\omega_{nm}t+\varphi_{nm}-n\chi(\rho)]} \qquad (14)$$

where $\omega_{nm} = n\omega_s - m\omega_r$, $\quad \varphi_{nm} = n\varphi_s - m\varphi_r$.

Using the result of Eqn. 14 and solving Eqn. 13 for the space charge field yields

$$E_{sc}(\vec{r},t) = E_q M \sum_{n,m=-\infty}^{\infty} J_n(\delta_{sig0}) J_m(\delta_{ref0}) \left[\frac{e^{i[\vec{K}\cdot\vec{r}+\Sigma+\frac{\pi}{2}+\omega_{nm}t+\varphi_{nm}-n\chi]}}{2(1+i\omega_{nm}\tau)} + c.c. \right] (15)$$

where *c.c.* stands for complex conjugate. Let

$$\tan(\psi_{nm}) = \omega_{nm}\tau, \quad \text{and} \quad \Theta_{nm} = \vec{K}\cdot\vec{r}+\Sigma+\frac{\pi}{2}+\omega_{nm}t+\varphi_{nm}-n\chi \quad \text{then}$$

$$E_{sc}(\vec{r},t) = E_q M \sum_{n,m=-\infty}^{\infty} J_n(\delta_{sig0}) J_m(\delta_{ref0}) \left[\frac{\cos[\Theta_{nm}] + \omega_{nm}\tau\sin[\Theta_{nm}]}{(1+\omega_{nm}^2\tau^2)} \right]$$

$$= E_q M \sum_{n,m=-\infty}^{\infty} J_n(\delta_{sig0}) J_m(\delta_{ref0}) \left[\frac{\sin[\vec{K}\cdot\vec{r} + \Sigma + \omega_{nm}t + \varphi_{nm} - n\chi - \psi_{nm}]}{\sqrt{1+\omega_{nm}^2\tau^2}} \right]. \tag{16}$$

This can be expanded to

$$E_{sc}(\vec{r},t) = E_q M \left[\begin{pmatrix} J_0(\delta_{sig0})J_0(\delta_{ref0}) \\ + \sum_{n=1}^{\infty} J_n(\delta_{sig0})J_n(\delta_{ref0}) \frac{\cos(n[\Omega t + \Phi - \chi] - \psi_n)}{\sqrt{1+n^2\Omega^2\tau^2}} \end{pmatrix} \sin(\vec{K}\cdot\vec{r}+\Sigma) \\ + \sum_{\substack{n,m=-\infty \\ (n \neq m)}}^{\infty} J_n(\delta_{sig0})J_m(\delta_{ref0}) \left(\frac{\sin[\vec{K}\cdot\vec{r}+\Sigma+(\omega_{nm}t+\varphi_{nm}-n\chi-\psi_{nm})]}{\sqrt{1+\omega_{nm}^2\tau^2}} \right) \right] \tag{17}$$

where the frequency difference $\Omega = \omega_s - \omega_r$, the phase difference $\Phi = \varphi_s - \varphi_r$, J_n is the Bessel function of the first kind and $\tan(\psi_n) = n\Omega\tau$. Eqn. 17 represents the electric space charge field within the photorefractive crystal as a series of terms including a constant term, low frequency terms at multiples of the difference frequency between the signal and reference beams and higher frequency terms at multiples of the signal and reference frequencies. In the above configuration, the photorefractive crystal acts as a mixing and low pass filtering element providing the benefits of lock-in detection. Therefore the space charge field responds to slowly varying phase modulations occurring within the material response time constant allowing only the terms around the difference frequency Ω to be important, assuming that $\Omega \ll \omega_{s,r}$. Employing the low pass filtering, Eqn. 17 for the space charge field becomes

$$E_{sc}(\vec{r},t) = E_q M \begin{bmatrix} J_0(\delta_{ref0})J_0(\delta_{sig0}(\rho)) \\ +2J_1(\delta_{ref0})J_1(\delta_{sig0}(\rho))\dfrac{\cos(\Omega t + \Phi - \chi(\rho) - \psi_1)}{\sqrt{1+\Omega^2\tau^2}} \\ +\dots \end{bmatrix} \sin(\vec{K}\cdot\vec{r}+\Sigma) \qquad (18)$$

which can be more compactly written as $E_{sc}(\vec{r},t) = E_q M f(\delta_{sig0}(\rho), \chi(\rho); t)\sin(\vec{K}\cdot\vec{r}+\Sigma)$.

The space-charge field modulates the local refractive index through the linear electro-optic effect. This effect creates a diffraction grating within the crystal that contains the low frequency phase information desired. Several methods can be used to readout the space charge field and diffraction grating including (1) four-wave mixing, (2) two-wave mixing with polarization selection, and (3) electrical measurement through conduction of photoexcited carriers. The magnitude of the index of refraction grating produced is given by[5] $n_1 = -\dfrac{n_0^3 r_{41} E_{sc}}{2}$, where n_0 is the average refractive index of the medium, r_{41} is the effective, orientation-dependent electro-optic coefficient in BSO. The diffracted beam intensity is a direct measure of the grating established and its diffraction efficiency is determined by the wave coupling constant, according to the scattering theory developed by Kogelnik,[21]

$$\zeta \equiv \left[\frac{\pi n_1 L}{\lambda\cos\theta}\right] = \left[\frac{\pi n_0^3 r_{41} E_q L}{2\lambda\cos\theta}\right] M f(\delta_{sig0}(\rho),\chi(\rho);t) = \frac{\Gamma L}{2} M f(\delta_{sig0}(\rho),\chi(\rho);t) \qquad (19)$$

where L is the interaction length, Γ is the two-wave mixing coupling constant[5] and $\Gamma L = 0.16$ for the BSO crystal used with input beam polarizations along the <001> and perpendicular to the <110> directions, λ is the laser source wavelength, and 2θ is the angle between the mixing waves.

J. Acoust. Soc. Am. 106, 2578-2587 (1999)

15

Operation in the four-wave mixing arrangement is described as it provides a simpler analysis for demonstrating the mechanism whereby lock-in imaging occurs since in this configuration there is no direct transmitted beam. The reference beam that passes through the crystal is reflected back into the crystal and diffracts from the photoinduced grating retracing the signal beam path, see figure 1. In the undepleted pump approximation, the diffracted (conjugate) beam intensity is[21]

$$I_4 = I_3 e^{-\alpha L/\cos\theta} |\sin\zeta|^2 \tag{20}$$

where I_3 is the back propagated reference beam intensity and α is the material absorption coefficient. The refractive index modulation amplitude generated by the mixing process is generally small, so that $\zeta \ll 1$, and $\sin(\zeta) \approx \zeta$. The intensity of the diffracted conjugate beam is given by

$$\frac{I_4}{I_3 e^{-\alpha L/\cos\theta}}$$
$$= \left(\frac{\Gamma L}{2}\right)^2 M^2 \left[\begin{array}{l} J_0^2(\delta_{ref0})J_0^2(\delta_{sig0}) + \\ \left[\dfrac{4J_0(\delta_{ref0})J_1(\delta_{ref0})}{\sqrt{1+\Omega^2\tau^2}} \right] J_0(\delta_{sig0})J_1(\delta_{sig0})\cos(\Omega t + \Phi - \chi(\rho) - \psi) + \dots \end{array} \right] \tag{21}$$

where $\tan(\psi) = \Omega\tau$. Eqn. 21 shows that the magnitude and phase of the traveling wave have been placed as arguments of the Bessel functions for the magnitude and as the phase of a low frequency AC signal. The resultant measured intensity is then proportional to

$$I_{AC} \propto J_0(\delta_{sig0})J_1(\delta_{sig0})\cos(\Omega t + \Phi - \chi(\rho) - \psi) \tag{22}$$

which for small traveling wave displacement amplitudes becomes

$$I_{AC} \propto \frac{\delta_{sig0}}{2} \cos(\Omega t + \Phi - \chi(\rho) - \psi) \quad \propto \left(\frac{1}{2}\right) \frac{4\pi\xi_0 |h(k_a\rho)|}{\lambda} \sin(\Omega t + \Phi - \chi(\rho) - \psi + \frac{\pi}{2})$$

$$\propto \frac{4\pi\xi(\rho, \Omega t + \vartheta - \chi(\rho))}{\lambda}, \quad \text{with} \quad \vartheta = \Phi - \psi + \frac{\pi}{2}. \tag{23}$$

Therefore, if Eqn. 23 is compared with Eqn. 9, the optical imaging approach can be seen to provide a true measure of the traveling wave amplitude and phase, for small amplitudes where $\dfrac{4\pi\xi(\rho,t)}{\lambda} << 1$.

The maximum measured intensity of Eqn. 22 occurs at a phase shift of 1.08 radians, which corresponds to a traveling wave amplitude of 45.7 nm for a probe wavelength of 532 nm. Comparison of the AC and DC terms in Eqn. 21, with knowledge of the reference beam modulation amplitude and the photorefractive crystal time constant, allows absolute calibration of the flexural wave displacement amplitude even when the maximum signal beam modulation amplitude cannot be realized.[22] Operation with the two-wave mixing method provides similar results whereby the diffraction process produces an output beam whose AC intensity component is proportional to the elastic wave displacement. This mode can be more efficient than the four-wave approach in that the output can be configured to be proportional to the two-wave mixing coupling constant Γ, rather than the square of this quantity. The analysis is complicated by the fact that a large directly transmitted beam is also present and does not further illustrate the lock-in measurement process under discussion; therefore, it is not presented here but will be the subject of future work.

SINGLE POINT MEASUREMENTS

Single point measurements were implemented with the two-wave mixing technique according to figure 1 by focusing the signal beam to a spot size of about 0.1 mm diameter onto a 0.125 mm thick pure nickel plate. A piezoelectric transducer with a short length of metal rod ground to a point served as the source transducer. The tip of the rod was placed in contact with the plate surface by applying a small amount of pressure and its vibration generated flexural waves in the plate. The plate was clamped at the outer plate boundaries between two pieces of a viscoelastic damping material[23] that shows damping characteristics superior to natural rubber. Continuous excitation of the transducer then produced steady traveling waves emanating from the contact point at a prescribed signal frequency and wavelength according to Eqn. 6. Although this method of excitation was suitable for the measurements here, difficulties were encountered due to the resonant behavior of the metal rod/transducer combination that allowed only discrete frequencies to be investigated. Figures 2-4 show the flexural wave amplitudes as a function of distance from the source for frequencies of 8.0, 15.0, and 30.0 kHz. The points are the result of direct measurement by translating the detection beam along a radius from the source point. The solid lines shown in the figures are the calculated results from Eqn. 6. Good agreement is seen between the measurements and the calculation using only the displacement amplitude at the source point and the relative phase between the signal and reference beam modulations as adjustable parameters. Some deviation is seen in the 8 kHz data at the left of figure 2 that we attribute to insufficient damping of the wave reflected from the supporting clamp at the plate edge. Material elastic and physical constants of

$$E = 204 \, GPa, \quad s = 0.31, \quad \rho_m = 8.9 \frac{g}{cm^3} \text{ and } h = 0.125 \text{ mm}$$ were used for the nickel plate

calculation. In each figure, both the traveling flexural wave displacement amplitude and phase were recorded by using AC lock-in measurement techniques. Figures 2-4 show the reconstructed waveforms taking into account the amplitudes and phases measured by the lock-in; the results are

proportional to the out-of-plane displacement, no absolute calibration was performed. The sensitivity of the measurement was ultimately limited by optical phase noise produced by the detection laser and environmental vibrations which had previously been shown to correspond to a minimum detectability of about 0.002 nm for these point measurements.[9] At each frequency, the relative phase shift between the signal and reference beams was adjusted so that the maximum displacement amplitude occurred at the source point yielding the results shown. Each figure corresponds to a snapshot of the traveling wave displacement along the plate at a moment in time. The wavelength of the flexural wave can be obtained by Fourier transforming the data and employing Eqn. 4. Measurements up to 1 MHz agreed well with the calculations, as shown in figure 5.

PHOTOREFRACTIVE DYNAMIC HOLOGRAPHIC IMAGING

Since optical interference and the photorefractive effect occur throughout the photorefractive crystal, the point method described above can be generalized to that of an image of the vibration over the surface of the plate. The volume character of the photorefractive process creates a grating distribution that locally records the phase modulation measured from each point of the specimen surface as long as the surface is accurately represented within the photorefractive crystal. The output beam intensity can then be measured by an array of detectors, or a highly pixelated device, such as a CCD camera. Each pixel records the local intensity from a point on the specimen producing an output proportional to that point's displacement. Even a diffusely reflecting surface can be measured if the surface is adequately imaged inside the photorefractive crystal by suitable optics.

The experimental setup for vibration imaging using polarization rotation through anisotropic self-diffraction is similar to that shown in figure 1 except that additional optical elements are used to illuminate and image the vibrating surface. A two-wave mixing configuration was used as the rough surface of the plate diffusely scattered the laser light resulting in insufficient light approaching the

video camera after diffracting from the grating in the four-wave method. Light from a solid state laser

source (532 nm, 1W), was split into two legs forming the signal and reference beams. The signal

beam was expanded and reflected off the surface of the plate undergoing continuous vibration.

Traveling flexural waves in the plate were excited by a contact piezoelectric transducer in the same

manner as with the point measurements. Light scattered from the plate was imaged in the

photorefractive crystal by a collection lens. The modulated reference beam was also expanded and

projected into the photorefractive crystal to produce the volume holographic grating. An input high

extinction ratio polarizer selected one component of the signal beam from the plate. At the output of

the crystal, the diffracted wavefront was selected through use of another high extinction ratio

polarizer.

Figure 6 shows images of the traveling flexural waves in the plate obtained with the two-wave

mixing method at frequencies of 8,15, and 30 kHz. The expected circular wavefronts due to the

isotropic microstructure of the nickel plate are clearly defined and the relative vibration

displacement phase is readily distinguishable. The figure shows single frame image data at three

different frequencies that have the background subtracted. For qualitative inspection of two

dimensional waveforms from the CCD output, the eye integrates over multiple video frames. If the

difference frequency is held at zero or locked to the camera frame rate of 30 Hz, a stationary

wavefront pattern is observed. This signal averaging makes it possible to easily detect subtle patterns

such as those brought about by the traveling waves. Also the entire pattern can be made to change its

phase continuously at the frequency, Ω, from 1-30 Hz, so that the appearance is that of waves

emanating from the center and traveling outward. This is physically equivalent to the actual

traveling wave motion except that viewing of the wave has been slowed to a much smaller

observation frequency that is held constant and independent of the actual wave frequency. A

sequence of successive frames is shown in figure 7. The frame rate is 30 Hz and the offset frequency

is about 4 Hz resulting in a continuous change in the relative phases between each image. The result is a time-lapse image that shows the viewer a wave emanating from the center and traveling outward and finally attenuated outside the field of view. This quasi-real-time imaging tells the viewer the wavefront shape from which information about the plate material, such as the elastic constants or the locations of flaws along the wave path can be determined.

The photorefractive process yields a true picture of the actual wave out-of-plane displacement motion and does not require any additional processing to generate the images of figure 6. However, to obtain quantitative measurement of the flexural wave displacement at any point within the image, the intensity at that point must be compared with the background value. This background value is obtained from an average of several additional frames recorded at different phase shifts between the signal and reference images phase locked so as to eliminate the flexural wave displacement when the average is taken. This procedure was previously illustrated in reference 9 concerning images of resonant vibrations in plates.

FREQUENCY ANALYSIS OF THE FLEXURAL WAVE IMAGES

The magnitude of the Fourier transform of the traveling wave displacement as a function of the radial propagation direction, Eqn. (4), shows a real pole at the applied wavevector for the traveling wave and imaginary poles of the same value that contribute to satisfy the boundary conditions. Therefore, the Fourier transform image of the traveling wave displacements should be a single ring at the applied wavevector delineating the propagating mode. Figures 8-10 show calculations and measurements of the traveling wave displacements as an image over the surface. The calculations are from Eqn. (6) and the measurements those of figure 6. Beside the images are shown images of the magnitude of the Fourier transforms. A strong response is seen as a ring at the propagating wavevector, whose magnitude can be determined to allow calculation of the elastic stiffness of the

plate, assuming the plate mass density per unit area is known. Both the wavefront and the Fourier transform images clearly show the isotropic character of the plate. Correspondingly, the figures also show the magnitude of the Fourier transforms of the measured image data. The large response is again seen as rings at the propagating wavevector values. This analysis procedure provides considerable information about the plate in one simple image.

ANISOTROPIC MATERIAL MEASUREMENTS

If the specimen is elastically anisotropic, then the wave speed varies with the propagation direction. Figure 11 shows this type of behavior for traveling waves in a sheet of carbon fiber composite. The carbon fiber sheet was approximately 0.18 mm thick with the fibers aligned in parallel along the vertical direction. The matrix is an isotropic resin material. The highly oblong wavefront pattern seen in figure 11 shows the anisotropy clearly and immediately. Figure 12 shows the wavelengths measured for this composite sheet in the directions along (x's) and perpendicular (o's) to the fibers as a function of frequency. Clearly, a great deal of information about the anisotropic elastic properties of the sheet can be obtained directly from this image measurement technique.

CONCLUSIONS

An imaging photorefractive optical lock-in traveling wave measurement method has been described. Detailed operation of the imaging method for recording nonstationary wavefronts through the lock-in process has been presented. Four-wave and two-wave mixing were described for reading out the signal producing an output intensity directly proportional to the amplitude of the vibration being measured at a preset mechanical phase. Point measurements scanned along a propagation radius produced a spatial snapshot of the amplitude and phase of the traveling waveform. Direct two-

dimensional surface images of the traveling wave were obtained by expanding the collection optics and imaging the output beam from the photorefractive material. These images showed the ultrasonic wavelength and wavefront shape and provided a quantitative method for obtaining the elastic stiffness symmetry of sheet materials, as illustrated for an isotropic nickel plate and an anisotropic composite carbon sheet. The method is capable of flat frequency response over a wide range above the cutoff of the photorefractive effect and is applicable to imaging the ultrasonic motion of surfaces with rough diffusely reflecting finishes.

ACKNOWLEDGMENTS

Figure Captions

Figure 1.   Photorefractive two-wave mixing setup for optical vibration detection.

Figure 2.   Flexural mode traveling wave surface displacement on a 0.125 mm thick nickel plate at 8.0 kHz.

Figure 3.   Flexural mode traveling wave surface displacement on a 0.125 mm thick nickel plate at 15.0 kHz.

Figure 4.   Flexural mode traveling wave surface displacement on a 0.125 mm thick nickel plate at 30.0 kHz.

Figure 5.   Flexural wave wavelengths as a function of driving frequency for the 0.125mm thick nickel plate, calculated (line) using parameters described in the text and measured (circles).

Figure 6.   Single frame images of the traveling waves at (top) 8 kHz, (middle) 15 kHz, and (bottom) 30 kHz.

Figure 7.   Time-lapse picture of successive frames of the traveling wave images showing the emergence of the wavefront from the center of the plate.

Figure 8.   Calculated (top) and measured (bottom) traveling wave displacements (left) and magnitude of the 2-D FFT (right) for the nickel plate at 8.0 kHz.

Figure 9.   Calculated (top) and measured (bottom) traveling wave displacements (left) and magnitude of the 2-D FFT (right) for the nickel plate at 15.0 kHz.

Figure 10.   Calculated (top) and measured (bottom) traveling wave displacements (left) and magnitude of the 2-D FFT (right) for the nickel plate at 30.0 kHz.

Figure 11.   Image of a traveling wave in a an anisotropic composite sheet at 37.8 kHz.

Figure 12.   Measurements of the wavelength in the vertical and horizontal directions in the anisotropic composite sheet.
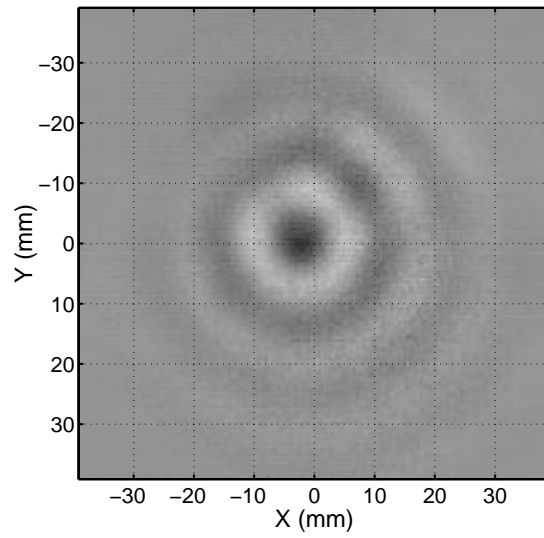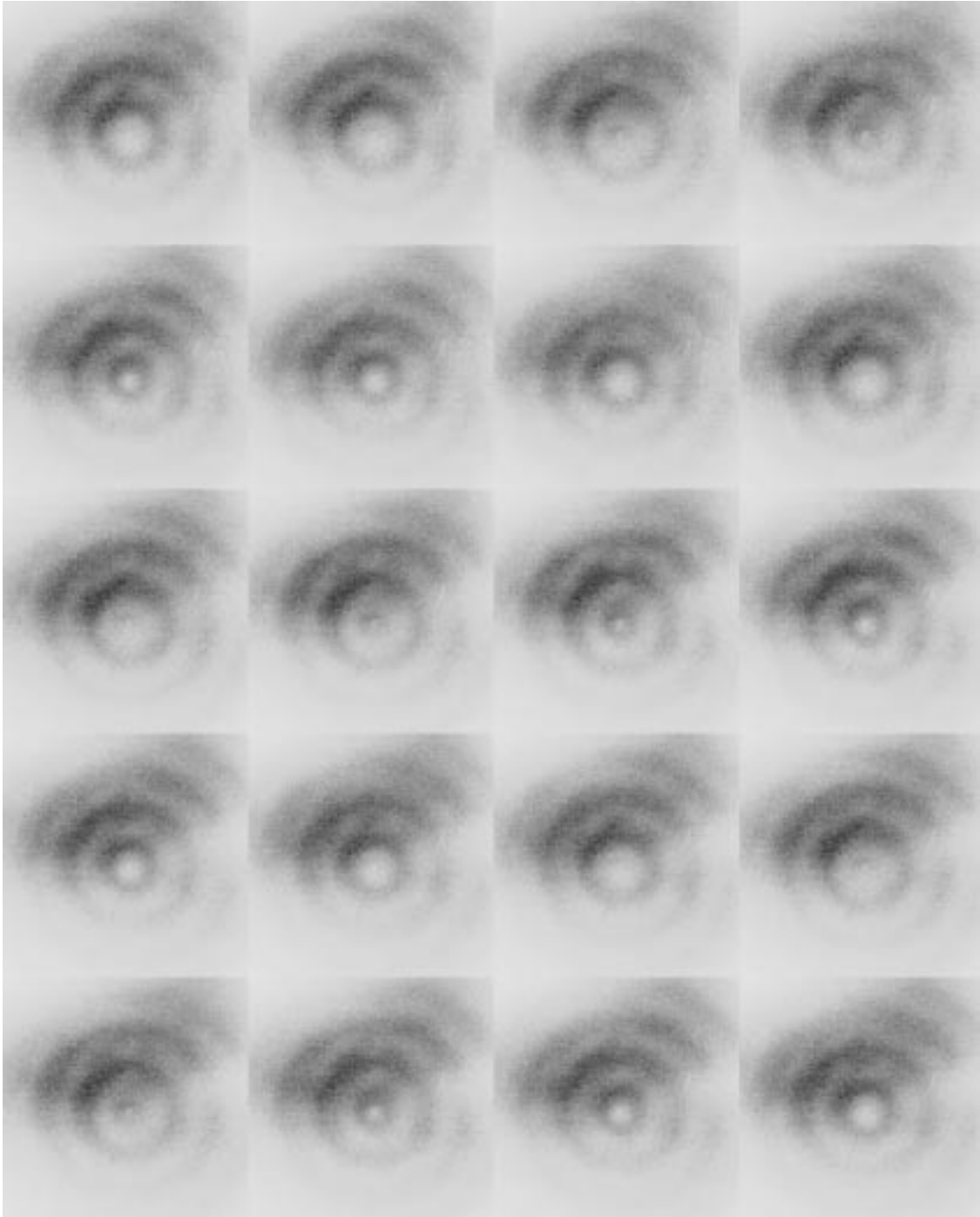
Laser

Sheet Specimen

δ_{ref}

2ζ

$\vec{K}$ $\vec{k}_r$

2θ

$\vec{\rho}$ $\vec{k}_a$

$\vec{k}_s$

$\vec{r}$

$\xi_o(\omega_s t)$

Signal Beam

$\vec{r}_s$

Piezoelectric
Transducer

$\delta_{sig} = \dfrac{4\pi\, \xi(\rho, \omega_s t)\, \cos(\zeta)}{\lambda}$

$\vec{r}_r$

Reference Beam

Photorefractive
Material

Figure 1

Figure 2   26

Figure 3

Figure 4

28

Figure 6

Figure 7
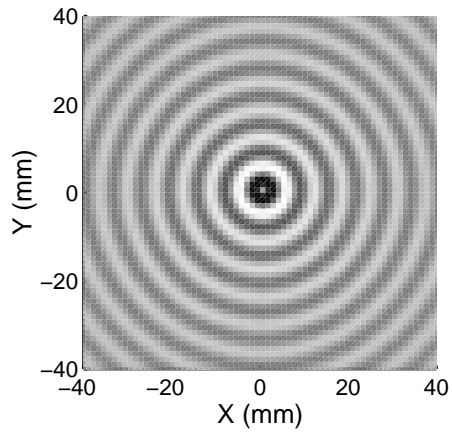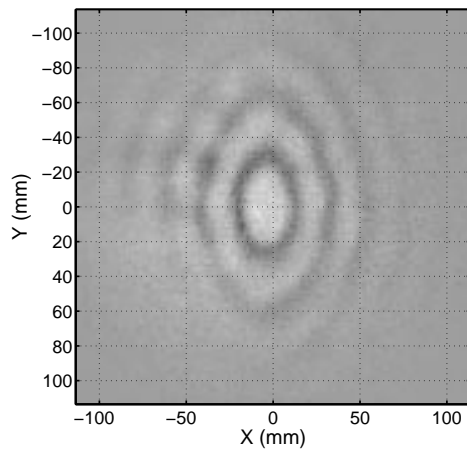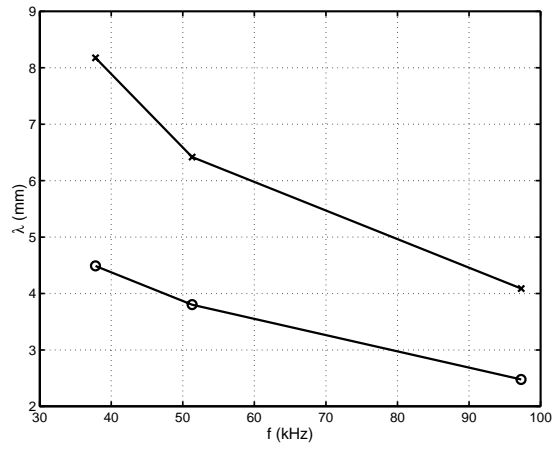
Figure 8

Figure 9

Figure 10

Figure 11

Figure 12
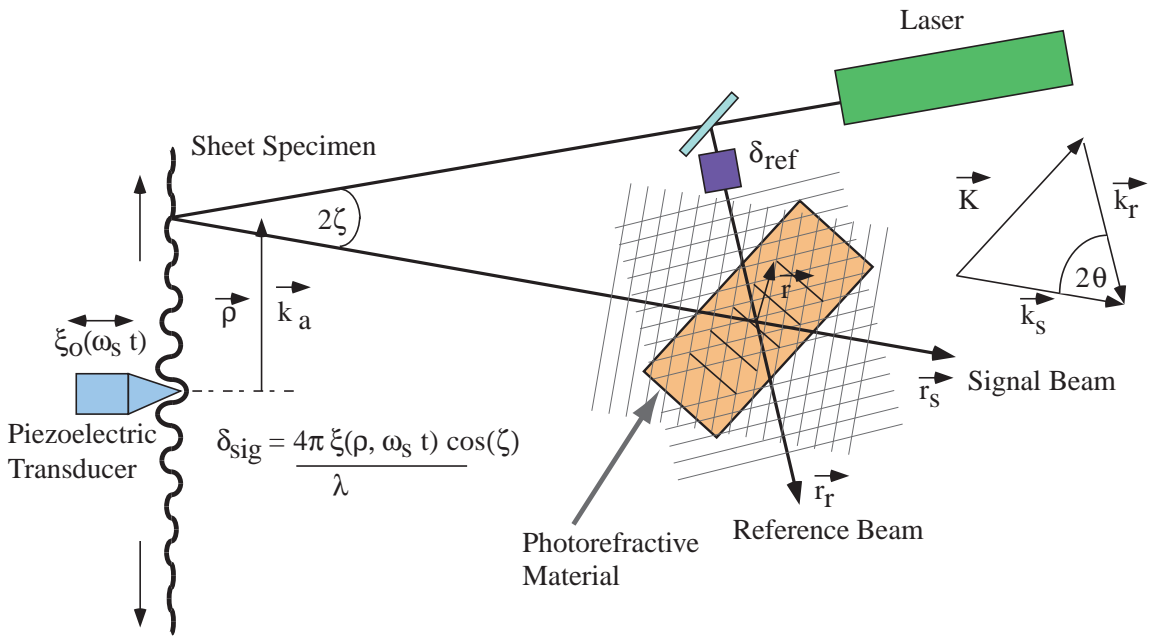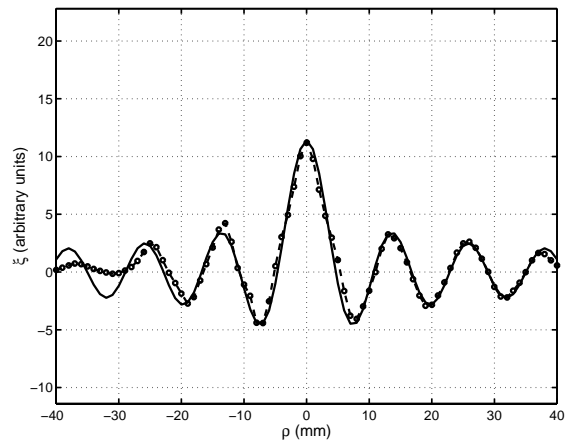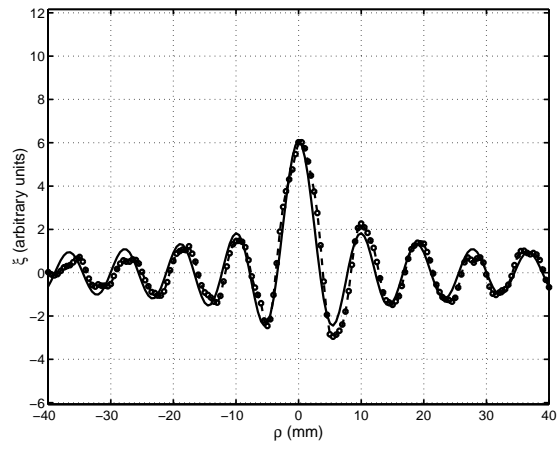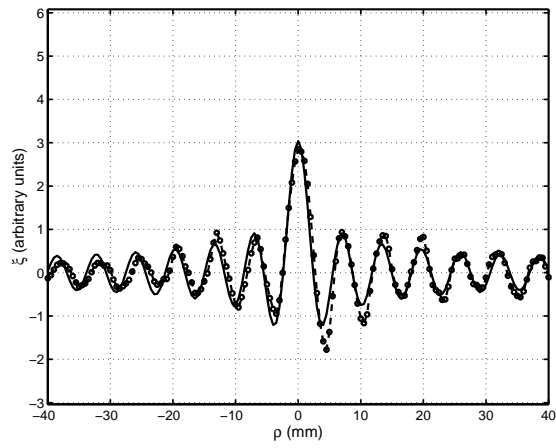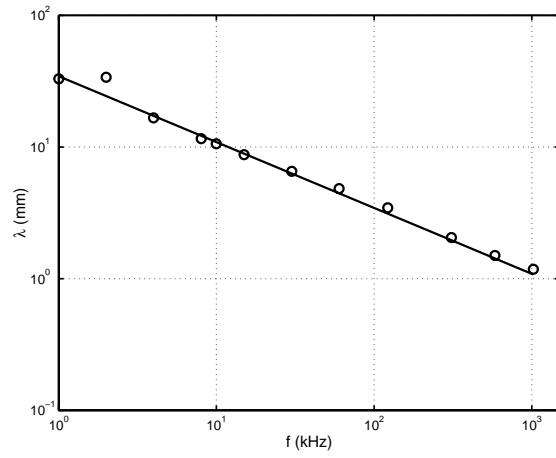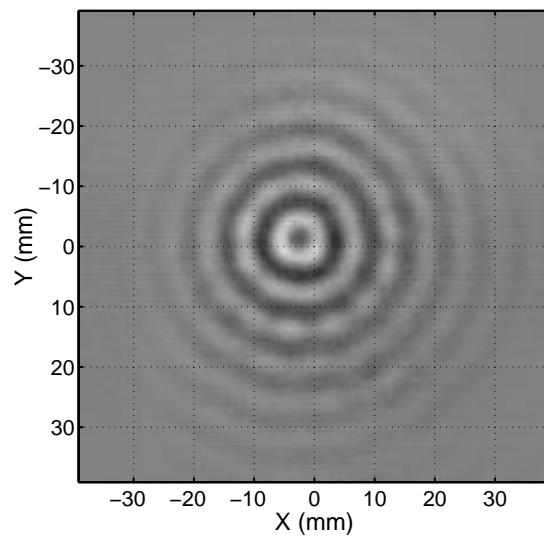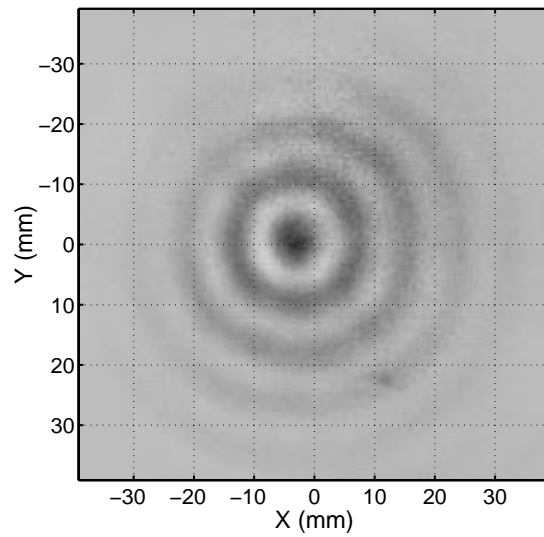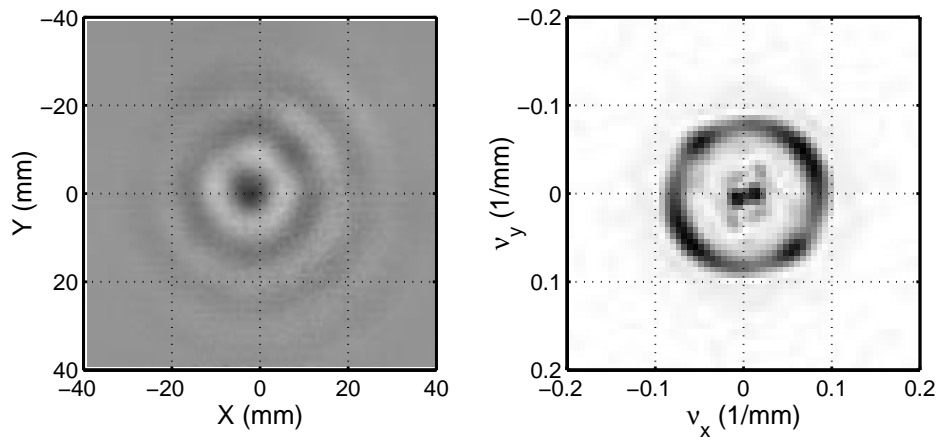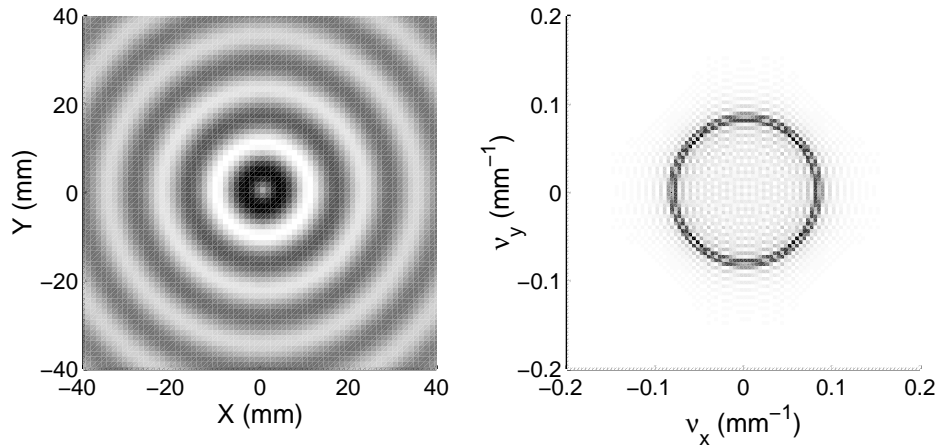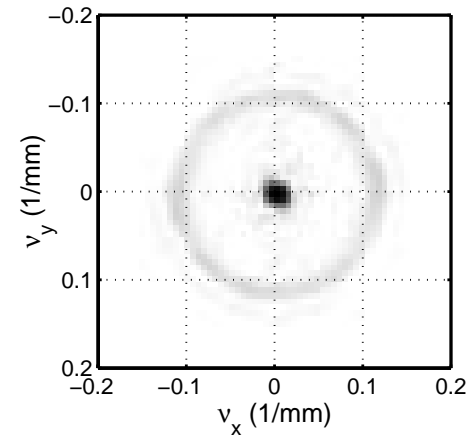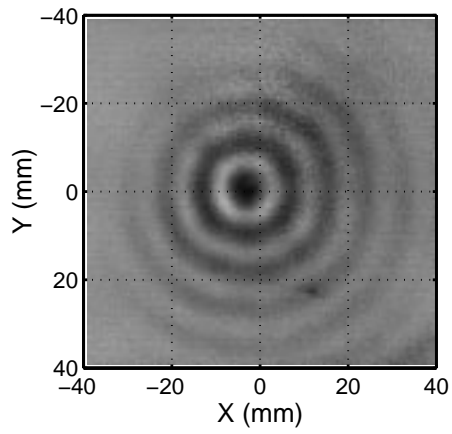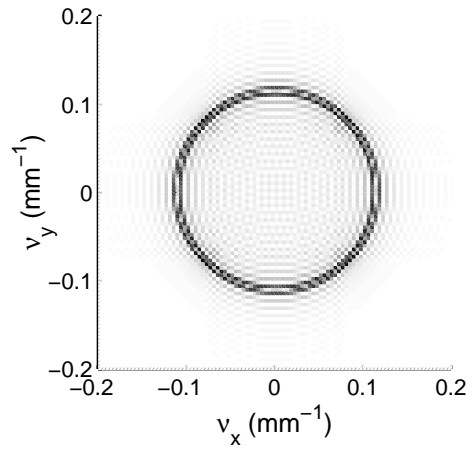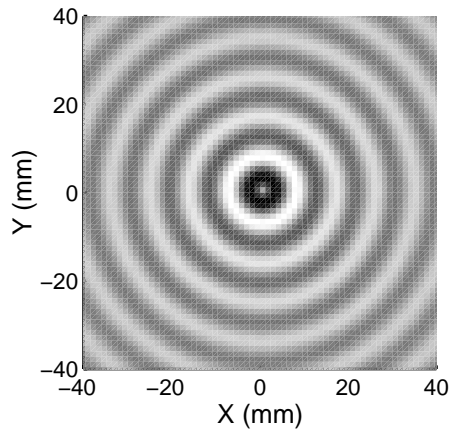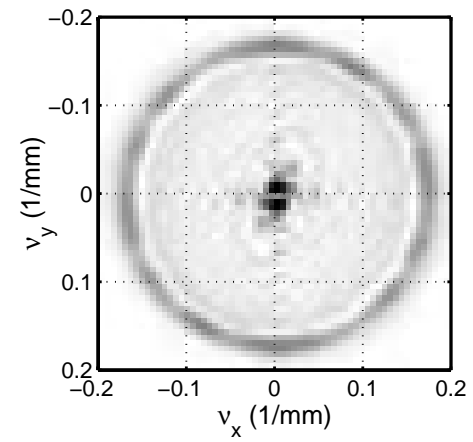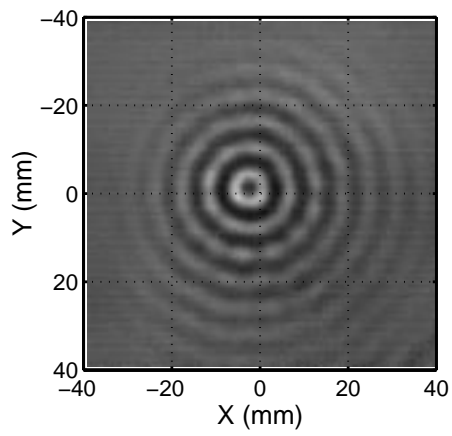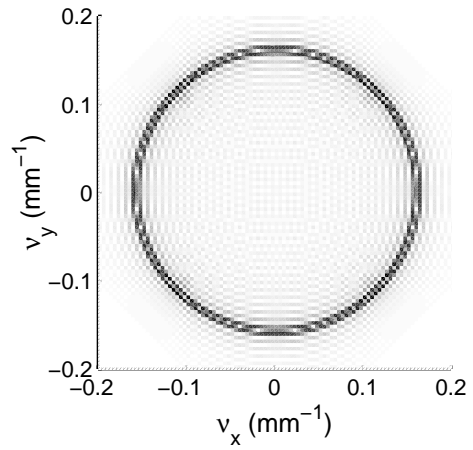
REFERENCES

[1] J. W. Wagner, *Physical Acoustics*, Vol.XIX, Eds. Thurston, R.N., and Pierce, A.D., (Academic Press, New York, 1990) Chp. 5.

[2] R. K. Ing and J.-P. Monchalin, Appl. Phys. Lett. 59, 3233 (1991).

[3] S. Ellingsrud and G.O.Rosvold, J. Opt. Soc. Am. A **9** (2), 237-251 (1992).

[4] B. A. Bard, G. A. Gordon, and S. Wu, J. Acoust. Soc. Am. 103 (6), 3327-3335, 1998.

[5] P. Yeh, *Introduction to Photorefractive Nonlinear Optics*, (John Wiley, New York, 1993).

[6] S. I. Stepanov, *International Trends inOptics*, Ed. By J. W. Goodman, (Academic Press, New York, 1991) Ch. 9

[7] T. C. Chatters and K. L. Telschow, *Review of Progress in QNDE*, Vol.15B, Eds. D.O. Thompson and D.E. Chimenti, (Plenum Press, New York, 1996) pp. 2165-2171.

[8] T.C. Hale and K. Telschow, Appl. Phys. Lett. 69, 2632-2634 (1996).

[9] T.C. Hale, K.L. Telschow and V.A. Deason, Applied Optics, 36, 8248 – 8258 (1997).

[10] K. L. Telschow, V. A. Deason, R. S. Schley and S. M. Watson, *Review of Progress in QNDE*, Vol.18A, Eds. D.O. Thompson and D.E. Chimenti, (Plenum Press, New York, 1999) pp. 999-1005.

[11] J. P. Huignard and A. Marrakchi, Opt. Lett., 6, (12), 622-624 (1981).

[12] H. Rohleder, P. M. Petersen and A. Marrakchi, J. Appl. Phys., 76 (1), 81-84 (1994).

[13] H. R. Hofmeister and A. Yariv, Appl. Phys. Lett., 61 (20), 2395-2397 (1992).

[14] R.C. Troth and J.C. Dainty, Opt. Lett., **16** (1), 53-55 (1991).

[15] K. E. Graff, *Wave Motion in Elastic Solids*, (Dover Pubs. Co., New York, 1991) Chapter 4.

[16] P. M. Morse and H. Feshbach, Methods of Theoretical Physics, (McGraw-Hill Book Co., New York, 1953) Part 1, Chapter 8.

[17] I.S. Gradshteyn and I.M. Ryzhik, Table of Integrals, Series, and Products, (Academic Press, new York, 1965) page 678.

[18] P.M. Morse and K. U. Ingard, *Theoretical Acoustics,* (McGraw-Hill, New York, 1968) 219

[19] Gradshteyn and Ryzhik, op. cit. page 956.

[20] J. Khoury, V. Ryan, C. Woods and M. Cronin-Golomb, Opt. Lett., **16**, 1442-1444 (1991).

[21] H. Kogelnik, "Coupled wave theory for thick hologram gratings," Bell System Technical Journal **48**, 2909-2947 (1969).

[22] K.L. Telschow, V. A. Deason, K.L. Ricks and R. S. Schley, ," *Nondestructive Characterization of Materials VIII,* ed. R. E. Green, Jr., (Plenum Press, New York, 1998) 79-84.

[23] Sorbothane, Inc., 2144 State Route 59 Kent, Ohio 44240